



Role of Lanthanide-Ligand bonding in the magnetization relaxation of mononuclear single-ion magnets: A case study on Pyrazole and Carbene ligated Ln^{III} (Ln=Tb, Dy, Ho, Er) complexes

TULIKA GUPTA, GUNASEKARAN VELMURUGAN, THAYALAN RAJESHKUMAR and GOPALAN RAJARAMAN*

Department of Chemistry, Indian Institute of Technology Bombay, Powai, Mumbai 400 076, India
e-mail: rajaraman@chem.iitb.ac.in

MS received 20 April 2016; revised 24 June 2016; accepted 6 July 2016

Abstract. *Ab initio* CASSCF+RASSI-SO+SINGLE_ANISO and DFT based NBO and QTAIM investigations were carried out on a series of trigonal prismatic M(Bc^{Me})₃ (M = Tb(**1**), Dy(**2**), Ho(**3**), Er(**4**), [Bc^{Me}][−] = dihydrobis(methylimidazolyl)borate) and M(Bp^{Me})₃ (M = Tb(**1a**), Dy(**2a**), Ho(**3a**), Er(**4a**) [Bp^{Me}][−] = dihydrobis(methylpyrazolyl)borate) complexes to ascertain the anisotropic variations of these two ligand field environments and the influence of Lanthanide-ligand bonding on the magnetic anisotropy. Among all the complexes studied, only **1** and **2** show large U_{cal} (computed energy barrier for magnetization reorientation) values of 256.4 and 268.5 cm^{−1}, respectively and this is in accordance with experiment. Experimentally only frequency dependent χ'' tails are observed for complex **1a** and our calculation predicts a large U_{cal} of 229.4 cm^{−1} for this molecule. Besides these, none of the complexes (**3**, **4**, **2a**, **3a** and **4a**) computed to possess large energy barrier and this is affirmed by the experiments. These observed differences in the magnetic properties are correlated to the Ln-Ligand bonding. Our calculations transpire comparatively improved Single-Ion Magnet (SIM) behaviour for carbene analogues due to the more axially compressed trigonal prismatic ligand environment. Furthermore, our detailed Mulliken charge, spin density, NBO and Wiberg bond analysis implied stronger Ln^{III}-H-BH agostic interaction for pyrazole analogues. Further, QTAIM analysis reveals the physical nature of coordination, covalent, and fine details of the agostic interactions in all the eight complexes studied. Quite interestingly, for the first time, using the Laplacian density, we are able to quantify the prolate and oblate nature of the electron clouds in lanthanides and this is expected to have a far reaching outcome beyond the examples studied.

Keywords. Lanthanides; magnetic anisotropy; ligand field environment; QTAIM and wiberg bond index analysis; single ion magnets.

1. Introduction

Since last two decades, lanthanide {Ln^{III}}^{1–13} containing complexes have become ubiquitous in the field of single molecule magnets (SMMs) having potential application in magnetic data storage.^{14–17} This is essentially due to their inherently large single-ion anisotropy arising from their deeply buried 4f orbitals, large unquenched orbital angular momentum and large number of unpaired electrons. Ln^{III} SMMs are preferred over their corresponding transition metal analogues as former result in larger effective energy barrier^{3,4} for magnetization reorientation (U_{eff}) upon Arrhenius fitting of the temperature dependence of relaxation time. Due to the large single-ion anisotropy of 4f metal

ions, even systems containing only one spin carrier {Ln^{III}} within a molecule are exhibiting magnetization blockade and these are termed as Single Ion Magnets (SIMs).^{5,18–34} Importance of magnetic anisotropy in the area of SMMs and ease of fine tuning it in mononuclear complexes has made the role of SIMs indispensable. Despite the tremendous progress in the area of SMMs and SIMs, they function only at very low temperatures (below liquid helium temperatures). Hence, in the quest of improved SIM characteristics, fine tuning of magnetic anisotropy and search/design of SIMs which are functional at room temperature^{35,36} is imperative.

Lack of uniaxiality/presence of perturbations, *i.e.*, transverse magnetic field led to mixing of opposite angular momentum projection, and this subsequently results in enhanced Quantum Tunneling of Magnetization (QTM) as well as poor SMM characteristics. Crystal field^{23,24,27,37–44} of the surrounding ligands essentially

*For correspondence
Celebrating 100 years of Lewis Chemical Bond

dictate the magnetic properties in SIMs entailing the need to fine tune ligand field strength towards novel targeted design of SIMs. Alongside, coordination number^{1,45-48} around the metal ion, coordination geometry/environment,⁴⁹ nature of the coordinated ligand and local point group symmetry need to be targeted simultaneously in order to achieve large U_{eff} values. The control of magnetic properties *via* structural, electronic feature as well as ligand field surroundings complicates the spin dynamics in SIMs and necessitates profound understanding of these issues. Recently,⁵⁰ crucial role of 4f electron density distributions of Ln^{III} ions have been proposed in an electrostatic manner to synthesize complexes towards stabilization of higher angular momentum energy levels. This explicitly suggests use of axial ligand field to stabilize largest angular momentum projections for oblate ions $\{\text{Tb}^{\text{III}}, \text{Dy}^{\text{III}} \text{ and } \text{Ho}^{\text{III}}\}$ and equatorial ligand field is preferred in prolate ions $\{\text{Er}^{\text{III}} \text{ and } \text{Yb}^{\text{III}}\}$. Hence, 4f electron density, corresponding crystal field parameters, magnitude of angular momentum also need to be modulated simultaneously in order to gain deeper insights into the magnetic anisotropic properties in Ln^{III} based SIMs.⁵⁰

Extensive experimental studies (Inelastic Neutron Scattering, HF-EPR, Angular Overlap Model)^{39,51-54} have been utilized to probe magnetic anisotropy, but sufficient knowledge about the directions of local anisotropy axes could not be obtained. Fragment quantum chemistry calculations can be a good alternative in this regard as it accounts for spin-orbit coupling non-perturbatively. It enables determination of orientation of local anisotropy axis of the metal ion through estimation of g-tensors of the ground multiplet of the Ln^{III} ions. CASSCF+RASSI-SO+SINGLE_ANISO methodology has proved its aptness in such kind of studies and verified experimentally observed magnetic data nicely.^{23,41,43,48,49,55-78}

Recently,⁷⁹ Long *et al.*, reported isostructural series of trigonal prismatic $\text{M}(\text{Bc}^{\text{Me}})_3$ ($\text{M} = \text{Tb}(\mathbf{1}), \text{Dy}(\mathbf{2}), \text{Ho}(\mathbf{3}), \text{Er}(\mathbf{4})$), $[\text{Bc}^{\text{Me}}]^-$ = dihydrobis(methylimidazoly)borate) and $\text{M}(\text{Bp}^{\text{Me}})_3$ ($\text{M} = \text{Tb}(\mathbf{1a}), \text{Dy}(\mathbf{2a}), \text{Ho}(\mathbf{3a}), \text{Er}(\mathbf{4a})$) $[\text{Bp}^{\text{Me}}]^-$ = dihydrobis(methylpyrazoly)borate) complexes. Concrete experimental magnetic techniques showed slower relaxation of magnetization for N-heterocyclic carbenes $\{\text{M}(\text{Bc}^{\text{Me}})_3\}$ -based lanthanides as compared to their isomeric pyrazole $\{\text{M}(\text{Bp}^{\text{Me}})_3\}$ ligands-based lanthanide analogues, suggesting better SIM behavior for the former. However, only for complexes $\text{Tb}(\text{Bc}^{\text{Me}})_3$ ($\mathbf{1}$) and $\text{Dy}(\text{Bc}^{\text{Me}})_3$ ($\mathbf{2}$), frequency as well as temperature dependence of χ'' component of magnetic susceptibility was detected. Complexes $\mathbf{1}$ and $\mathbf{2}$ show relaxation of magnetization with U_{eff} values of 44.8 cm^{-1} (Yttrium diluted sample showed 45.2 cm^{-1}) and 32.8 cm^{-1}

(Yttrium diluted sample showed 33.6 cm^{-1}), respectively, under an applied dc magnetic field of 1500 Oe (field induced SIM, f-SIM behaviour).⁷⁹ On the other hand, only high frequency χ'' tails are experimentally observed for complexes $\mathbf{1a}$ and $\mathbf{2a}$ at an applied dc magnetic field of 1250 Oe with small U_{eff} of 21 cm^{-1} for $\mathbf{1a}$.⁷⁹ Such change in magnetic behavior upon changing the number of 4f electrons has spurred our interest towards explicit analysis of these complexes and the nature of Ln-Ligand bonding. Therefore, here we have performed vigorous post-Hartree-Fock *ab initio* and DFT calculations on these eight complexes with an aim to answer the following intriguing questions: i) What are the origins of different energy barrier for magnetization reorientations in carbene- and pyrazole ligated complexes? ii) What is the mechanism of relaxation in these sets of complexes? iii) How structure and bonding features influence the magnetization blockade (Table 1)?

2. Computational

MOLCAS 8.0⁸⁰⁻⁸⁶ suite has been employed to perform post-Hartree-Fock *ab initio* calculations. Spin-free wave functions were generated using complete active space self-consistent field (CASSCF) method. These multi-configurational wave functions have been used as input states to account for spin-orbit coupling *via* Restricted Active Space Spin State Interaction-Spin Orbit (RASSI-SO) methodology.^{86,87} The resultant energies of the multiplets were used for the calculation of the anisotropic magnetic properties and g-tensors of the lowest state using a specially designed routine SINGLE_ANISO.⁸⁸ We have employed [ANO-RCC...7s6p4d2f1g.] basis set for Ln^{III} $\{\text{Ln}^{\text{III}} = \text{Tb}, \text{Dy}, \text{Ho}, \text{Er}\}$, [ANO-RCC...3s2p.] basis set for N,O,C and B, and [ANO-RCC...2s.] basis set for H throughout our calculations. These ANO-RCC basis sets were adopted from ANO-RCC basis library included in MOLCAS 8.0 suite. The active space of (8,7) is used for $\text{Tb}(\text{Bc}^{\text{Me}})_3$ ($\mathbf{1}$) and $\text{Tb}(\text{Bp}^{\text{Me}})_3$ ($\mathbf{1a}$) complexes. In the Configurational Interaction (CI) procedure, 7 septets, 140 quintets and 195 triplets are considered. The singlet states were not included due to computational limitations. In the RASSI module, 7 septets, 105 quintets and 112 triplets are mixed by spin-orbit coupling within the energy window of about $40,000 \text{ cm}^{-1}$. The active space (9,7) is adopted for $\text{Dy}(\text{Bc}^{\text{Me}})_3$ ($\mathbf{2}$) and $\text{Dy}(\text{Bp}^{\text{Me}})_3$ ($\mathbf{2a}$) complexes. Here, in the CI procedure, 21 sextets were considered and this was only mixed by spin-orbit coupling as it has been found to be robust for computing the g-tensors for Dy^{III} ions. The active space (10,7) is used for $\text{Ho}(\text{Bc}^{\text{Me}})_3$ ($\mathbf{3}$) and $\text{Ho}(\text{Bp}^{\text{Me}})_3$ ($\mathbf{3a}$) complexes. In

Table 1. Calculated energy spectrum, g-tensors, relative energies and angles (θ) of the principal anisotropy axes of first excited states with respect to the ground state for ground and first excited Kramers (for **2**, **2a**, **4**, **4a**) and pseudo doublets (for **1**, **1a**, **3** and **3a**) in **1–4** and **1a–4a**.

Ground multiplet	1	2	3	4	1a	2a	3a	4a
g_x	0	0.07	9.64	0.58	0	0.06	0	9.53
g_y	0	0.09	9.33	1.73	0	0.08	0	9.61
g_z	17.93	19.91	1.08	3.66	17.92	19.91	16.92	0.81
Energy (cm ⁻¹)	0.0 and 0.02	0.0	0.0 and 0.04	0.0	0.0 and 0.05	0.0	0.0 and 0.07	0.0
1 st excited multiplet	1	2	3	4	1a	2a	3a	4a
g_x	0	0.01	0.08	0.51	0	0.24	0	0.35
g_y	0	0.18	0.24	0.70	0	0.38	0	0.68
g_z	14.65	17.31	3.17	3.77	14.66	17.26	14.37	2.14
Energy (cm ⁻¹)	256.36 and 256.39	7.27	9.01 and 12.05	23.29	229.39 and 229.44	23.19	13.08 and 25.43	5.63
angle(°)	0.01	2.73	0.01	0.71	0.01	0.35	0.34	8.28
U_{cal} (cm ⁻¹)	256.36	268.50*	9.01	23.29	229.39	23.19	13.08	5.63
U_{eff} (cm ⁻¹)	44.8(45.2)	32.8(33.6)	–	–	21	–	–	–

*Barrier with respect to the fourth excited KD; Values within bracket in U_{eff} row represent experimentally estimated energy barrier for Yttrium diluted samples.

the configurational Interaction (CI) procedure, 35 quintets, 210 triplets and 196 singlets are considered. In the RASSI module, 35 quintets, 118 triplets and 76 singlets and 30 quintets, 107 triplets and 38 singlets for **3** and **7** respectively are mixed by spin-orbit coupling within the energy window of about 40,000 cm⁻¹. The active space (11,7) is adopted for Er(Bc^{Me})₃ (**4**) and Er(Bp^{Me})₃ (**4a**) complexes. In the configurational Interaction (CI) procedure, 35 quartets and 112 doublets are considered. In the RASSI module, 35 quartets and 112 doublets for both the Er^{III} complexes are mixed by spin-orbit coupling within the energy window of about 40,000 cm⁻¹. Mulliken charges and the spin densities have been computed using DFT calculations employing Gaussian 09⁸⁹ suite. Here we have employed the B3LYP functional, along with the CSDZ⁹⁰ basis set for the Ln^{III} ion and the Ahlrichs triple- ζ ⁹¹ basis set (TZV) has been employed for the rest of the atoms.

The wave function for use in quantum theory of atoms in molecules (QTAIM) analysis were generated from single point calculation using hybrid B3LYP functional^{92–94} with a combination of CSDZ⁹⁰ ECP on Tb, Dy, Ho, Er and TZV Ahlrichs triple- ζ basis set on other atoms as implemented in the Gaussian 09 suite⁸⁹ of programs. Further, the quantum theory of atoms in molecule (QTAIM) was applied to depict the topological properties of the chosen complexes. To better understand the nature of the interaction of the Ln atom with others, we have used the Baders Atoms in Molecules theory.⁹⁵ In this theory, Bader and co-workers characterize bonding and non-bonding interactions of atoms in terms of topological properties such as electron density $\rho(r)$, Laplacian of the electron density $L(r)$, potential energy density $V(r)$, kinetic energy density $H(r)$ and a

potential energy to the Lagrangian kinetic energy ratio ($V(r)/G(r)$). For instance, the presence of a (3, -1) critical point in QTAIM topography represents a chemical bond between two atoms and are called as the bond critical points (BCPs) where the shared electron density reaches a minimum, whereas a critical point with (3, +1) and (3, +3) signatures identify a ring structure (RCP) and cage critical point (CCP) in the molecular system. The $\rho(r)$ values at the BCPs are related to the strength of the bonds.⁹⁶ In this study, QTAIM calculations are performed at B3LYP/CSDZ level using AIM2000 package.⁹⁷

3. Results and Discussion

We have chosen eight isostructural and isomeric complexes **1–4** and **1a–4a** for our study. All the complexes comprise six coordinate Tb^{III}, Dy^{III}, Ho^{III} and Er^{III} in tricapped trigonal prismatic coordination environment surrounded by three pyrazolate ligands in complexes **1a–4a** and three N-heterocyclic carbene ligands in complexes **1–4**. Among the lanthanide family, Dy^{III} ion has indisputably led to the largest number of pure SIMs. This is ascribable to the reduced QTM of these systems compared to other lanthanide ions owing to its large magnetic moment and odd electron configuration. Here, we begin our discussion with single-ion magnetic behaviour in all the complexes followed by cross comparison between lanthanide complexes.

3.1 Single-ion anisotropy studies on complexes **1** and **1a**

The energy spectrum for thirteen energy states (six pseudo-doublets and one singlet) of the ground ⁷F₆

multiplet for the Tb^{III} ion and g -tensors of ground state in compounds **1** and **1a** are shown in the Supplementary Information (SI), with the excited states lying at 2400 cm^{-1} . As expected for the non-Kramers ion, all the pseudo-doublets in complexes **1** and **1a** are pure Ising in nature. Ground pseudo-doublet for **1** and **1a** possesses g_z value of 17.93 and 17.92 (see ground state g_z orientation in Figures 1a and 1b), respectively, approaching that expected for pure $m_j = \pm 6$ state of $g_z \sim 18$. See Tables S3 and S4 in Supplementary Information. Tunnel splitting (Δ_{tun}) within the ground multiplets is considerable for both the complexes (0.02 and 0.05 cm^{-1} for **1** and **1a**, respectively; larger than the cut-off value of 10^{-5} cm^{-1} (Table 1)) suggesting absence of magnetic bistability. This precludes zero-field SIM behaviour for both the complexes. However,

application of dc field enhances the ground-first excited level gap posing probable SIM characteristics on both the compounds by quenching QTM probability. Our calculations affirm tunnel splitting of 0.03 and 0.04 cm^{-1} , respectively, for **1** and **1a** in their corresponding first excited pseudo-doublets. This outlines calculated energy barrier (U_{cal}) to be 256.4 and 229.4 cm^{-1} for **1** and **1a** (Table 1), respectively to promote relaxation *via* this level. This represents both **1** and **1a** to be SIM. In complex **1**, our calculations overestimate the experimentally observed U_{eff} value of 44.8 (45.2) cm^{-1} and this can be ascribed to the lack of consideration of intermolecular interaction and zero-field QTM in our calculations.

However, though complex **1a** shows large U_{cal} of 229.4 cm^{-1} , frequency tails (χ'') at field of 1250 Oe

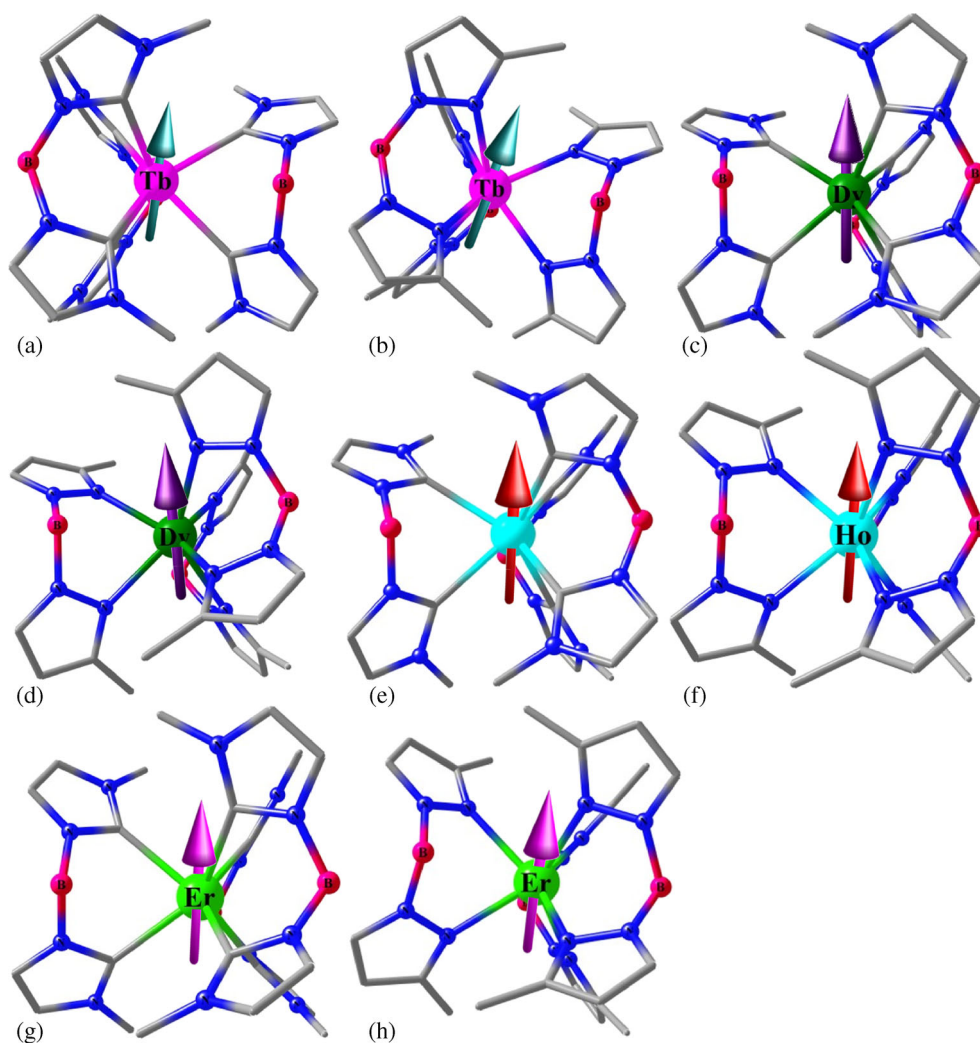


Figure 1. *Ab initio* computed orientation of g_z -tensor for ground state KD in complexes. (a) **1**, (b) **1a**, (c) **2**, (d) **2a** (e) **3**, (f) **3a**, (g) **4** and (h) **4a**, as shown with their crystal structures $\{M(\text{Bc}^{\text{Me}})_3$ ($M = \text{Tb}(\mathbf{1})$, $\text{Dy}(\mathbf{2})$, $\text{Ho}(\mathbf{3})$, $\text{Er}(\mathbf{4})$, $[\text{Bc}^{\text{Me}}]^- = \text{dihydrobis(methylimidazolyl)borate}$) and $M(\text{Bp}^{\text{Me}})_3$ ($M = \text{Tb}(\mathbf{1a})$, $\text{Dy}(\mathbf{2a})$, $\text{Ho}(\mathbf{3a})$, $\text{Er}(\mathbf{4a})$, $[\text{Bp}^{\text{Me}}]^- = \text{dihydrobis(methylpyrazolyl)borate}$)}. Color scheme: Tb: red, Dy: dark green, Ho: sky blue, Er: light green, O: red, N: blue, C: grey. H atoms have been removed for clarity.

was experimentally observed leading to the estimation of U_{eff} as 21 cm^{-1} . Our wave function analysis reveals ground state as a admixture of $70\% |\pm 6\rangle$ and small contributions from other m_j levels for **1** and **1a**. Ground state axial crystal field parameters are much larger ($B_2^0 = 5.47$ and 4.75 for **1** and **1a** respectively) than the corresponding non-axial terms ($B_2^{-1,+1}$) (see Table S9 in SI). This accounts for the pure Ising nature, resulting from the non-Kramer Tb^{III} ion in complexes **1** and **1a**. For both the compounds, g_z orientation intersects through the negatively charged three ligands in order to encounter least electrostatic repulsion (Figures 1a and 1b). Our computed data is further substantiated by nice agreement between calculated and experimental $\chi_{\text{m}}T$ vs T plots (Figures 3a and 3b).

3.2 Single-ion anisotropy studies on complexes **2** and **2a**

The energy spectrum for eight Kramers doublets of the ground ${}^6\text{H}_{15/2}$ multiplet for the Dy^{III} ion and g -tensors of ground state in compound **2** and **2a** are shown in the Supplementary Information, with the excited states lying at 3000 cm^{-1} . In **2** and **2a**, the ground state (GS) Kramers doublet (KD) shows almost Ising type anisotropy with $g_{xy} < 0.5$ (Tables S1 and S2 in Supplementary Information (Table 1)) *i.e.*, $g_z = 19.91$ *i.e.*, (see ground state g_z orientation in Figures 1c and 1d) close to that expected for a pure $m_j = \pm 15/2$ state of $g_z \sim 20$. It is worthy to note that, all the computed g -tensors correspond to an effective spin $\tilde{S} = 1/2$ of the KDs. For **2**, main anisotropic g -tensor (g_z) lies at lower angles ($< 3^\circ$) upto fourth excited KD. This opens up probabilities of magnetic relaxation *via* higher excited multiplets resulting in larger energy barrier for magnetization reorientation. It is notable that, transverse components of the energy multiplets are negligible upto third excited KD; $g_{xy} < 0.5$ and it becomes very prominent in fourth excited KD ($g_x = 5.1$; $g_y = 5.3$, $g_z = 8.0$). We have further analysed the relaxation mechanism which can occur *via* three pathways: a) QTM between the ground KDs owing to substantial transverse anisotropy of ground KDs; b) Orbach/Raman process to induce relaxation *via* excited KDs which is essentially controlled by non-collinearity of g_z axis; c) thermally assisted-QTM (TA-QTM) within excited KDs resulting due to non-Ising nature of excited KDs. In qualitative *ab initio* computed relaxation mechanism, the KDs are arranged in accordance with their magnetic moments. The numbers at each arrows (solid, dashed and dotted) connecting any two energy states correlate to the matrix elements of the transition magnetic moments between the respective energy levels. As the ground state is almost pure Ising type due to negligible

transverse anisotropy, QTM pathway is least effective *via* this state as reflected in computed magnetic moment of $0.03 \mu_B$. We would like to note here that matrix element connecting same multiplets of opposite directional magnetization having a value $> 10^{-1} \mu_B$ along with substantial transverse component ($g_{xy} \sim 4$) promotes relaxation *via* that particular state.^{14h} Similar trend of less efficient TA-QTM within excited states was evident ($\sim 0.05 \mu_B$) upto third excited KD due to negligible transverse anisotropy. Although pronounced magnetic moment corresponding to Orbach/Raman relaxation upto third excited KD ($\sim 3 \mu_B$) was computed, lower angle of the g_z alignment of excited KDs (upto third) with respect to ground KD and small transverse components deters relaxation *via* these states. Fourth excited KD possesses huge transverse anisotropy and this was corroborated by substantial TA-QTM pathway *via* this state ($1.76 \mu_B$) and a significant Orbach relaxation pathway ($3.09 \mu_B$). This essentially outlines the calculated energy barrier (U_{cal}) as 268.5 cm^{-1} (Figure 2a) with respect to the experimental U_{eff} value 32.8 (33.6) cm^{-1} for complex **2** (Table 1). This large discrepancy between U_{cal} and U_{eff} values have been observed earlier and are attributed to, (i) QTM effects which are not incorporated in the U_{cal} estimates, (ii) intermolecular/hyperfine interactions, and (iii) other relaxation mechanism such as Raman process being operational. Ising nature of the ground state is also corroborated by negligible QTM ($0.02 \mu_B$) in complex **2a** (Figure 2b). Now, complex **2a** reveals huge transverse anisotropy ($g_{xy} > 0.5$; $g_{xy} < 4$) in the first excited KD which is also reflected in pronounced TA-QTM ($0.10 \mu_B$). This outlines U_{cal} as 23.2 cm^{-1} which is in line with the experimentally observed high frequency tails (χ'') at field of 1250 Oe with no observed U_{eff} values.

Our wavefunction analysis is affirmative of $|\pm 15/2\rangle 99\% |\pm 15/2\rangle$, as ground state KD for both the complexes. However, fourth excited KD which involves in determining energy barrier is admixture of $56\% |\pm 7/2\rangle + 18\% |\pm 5/2\rangle$ states in complex **2**. In complex **2a**, first excited KD is pure $|\pm 13/2\rangle$: $94\% |\pm 13/2\rangle$ state. Ground state axial crystal field parameters are much larger ($B_2^0 = 3.28$ and 2.97 for **2** and **2a**, respectively) than corresponding non-axial terms ($B_2^{-1,+1}$) (Table S9 in SI). This suggests suppressed QTM within ground state for both the complexes reiterating our earlier statements. For both the compounds, g_z orientation intersects through the negatively charged three ligands in order to encounter least electrostatic repulsion (see Figures 1c and 1d). Our computed data is further substantiated by nice agreement between calculated and experimental $\chi_{\text{m}}T$ vs T plots (Figures 3c and 3d).

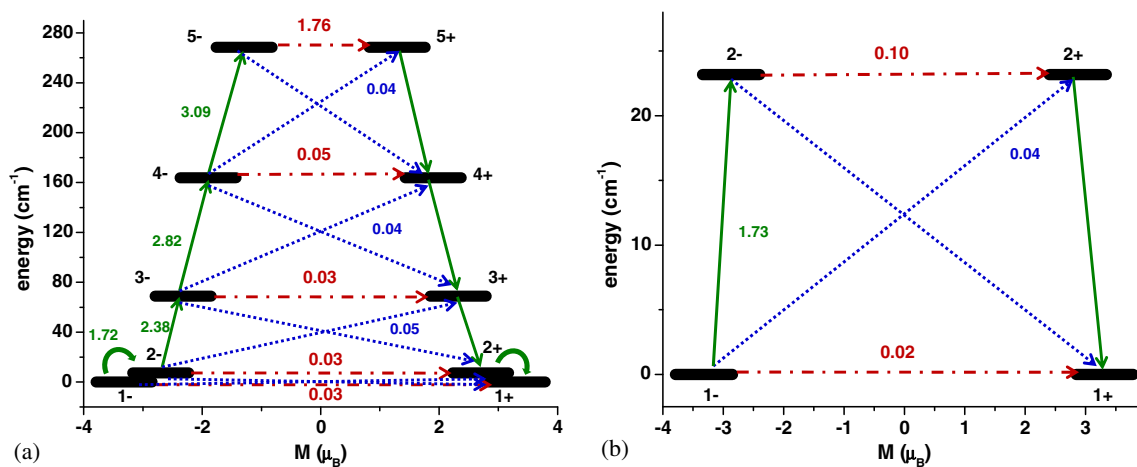


Figure 2. *Ab initio* calculated magnetization blocking barrier for complexes, (a) **2** and (b) **2a**. The thick black line represent the Kramer's doublets (KDs), as a function of magnetic moment. The blue dotted lines indicate the possible path for the Orbach process. The solid green arrows imply the most probable relaxation pathways for magnetization reversal. The dashed-dotted red lines correspond to the presence of QTM/TA-QTM between the connecting pairs. The numbers at each arrow are the mean absolute value for the corresponding matrix element of transition magnetic moment.

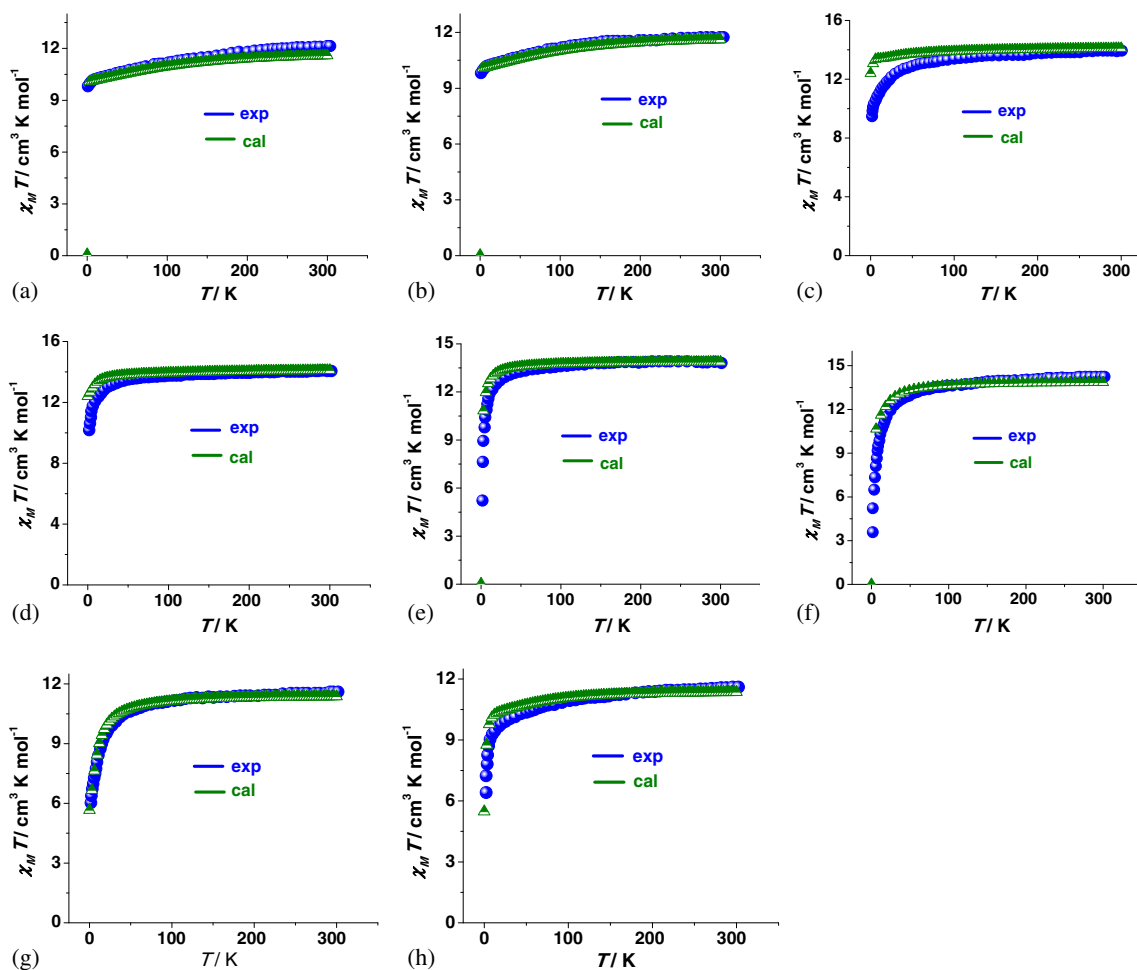


Figure 3. Experimental and *ab initio* calculated molar magnetic susceptibility plots for complexes; (a) **1**, (b) **1a**, (c) **2**, (d) **2a**, (e) **3**, (f) **3a**, (g) **4** and (h) **4a**. Here, blue filled circles represent data extracted from experimental plots while half-filled-half-void green triangles correspond to *ab initio* calculated molar magnetic susceptibilities. It is noteworthy, that intermolecular interaction zJ is assumed to be zero in these calculations.

3.3 Single-ion anisotropy studies on complexes **3** and **3a**

The energy spectrum for seventeen energy states (seven pseudo-doublets and three singlets) of the ground 5I_8 multiplet for the Ho^{III} ion and g -tensors of ground state in compound **3** and **3a** are shown in the Supplementary Information, with the excited states lying at $\sim 5200 \text{ cm}^{-1}$. As expected for the non-Kramers ion, all the pseudo-doublets in complexes **3** and **3a** are pure Ising in nature. Ground pseudo-doublet for **3** and **3a** possesses g_z of 17.10 and 16.92, respectively, (see ground state g_z orientation in Figures 1e and 1f), resembles that expected for pure $m_j = \pm 7$ state of $g_z \sim 17.5$, (Tables S5 and S6 in SI) but far from the pure $m_j = \pm 8$ state of $g_z \sim 20$. This is also corroborated by our computed wave function analysis which shows ground state composed of 70% $|\pm 7\rangle$ state with a small contributions from other m_j levels for both the complexes. Tunnel splitting (Δ_{tm}) within the ground multiplets is considerably large for both the complexes (0.04 and 0.07 cm^{-1} for **3** and **3a**, respectively; larger than the cut-off value of 10^{-5} cm^{-1} (Table 1)) suggesting absence of magnetic bistability. This precludes zero-field SIM behaviour for both the complexes. However, application of dc field enhances the ground-first excited level gap posing probable SIM characteristics on both the compounds by suppressing the extent of QTM effects.

Our calculations yield tunnel splitting of 3.04 and 12.35 cm^{-1} , respectively, for **3** and **3a** in their corresponding first excited pseudo-doublets. This large tunnelling gap indicates relaxation *via* this state with U_{cal} value of 9.01 and 13.08 cm^{-1} for **3** and **3a** (Table 1), respectively. Such small energy barrier value supports

experimental observation of the absence of χ'' peaks even in applied field conditions. This rules out the possibility of magnetic bistability as well as SIM behaviour. Ground state axial crystal field parameters are much larger ($B_2^0 = 1.00$ and 0.93 for **3** and **3a**, respectively) than corresponding non-axial terms ($B_2^{-1,+1}$) (Table S9 in SI). This accounts for the pure Ising nature resulting from the non-Kramer Ho^{III} ion in complexes **3** and **3a**. For both the compounds, g_z orientation intersects through the negatively charged three ligands in order to encounter least electrostatic repulsion (Figures 1e and 1f). Our computed data is further substantiated by nice agreement between calculated and experimental $\chi_m T$ vs T plots (Figures 3e and 3f).

3.4 Single-ion anisotropy studies on complexes **4** and **4a**

The energy spectrum for eight Kramers doublets of the ground $^4I_{15/2}$ multiplet for the Er^{III} ion and g -tensors of ground state in compound **4** and **4a** are shown in the Supplementary Information, with the excited states lying at 6600 cm^{-1} . In **4** and **4a**, the ground state (GS) Kramers doublet (KD) contains substantial transverse anisotropy; *i.e.*, $g_x = 9.64$, $g_y = 9.33$, $g_z = 1.08$ and $g_x = 9.53$, $g_y = 9.16$, $g_z = 0.81$ for **4** and **4a**, respectively (see ground state g_z orientation in Figures 1g and 1h) (See Tables S7 and S8 in SI) (Table 1). This is also substantiated by stabilization of $m_j = |\pm 1/2\rangle$: 57% $|\pm 1/2\rangle$ and $m_j = |\pm 1/2\rangle$: 59% $|\pm 1/2\rangle$ for **4** and **4a**, respectively. Analysis on magnetic relaxation mechanism exhibits pronounced QTM of 3.16 and $3.11 \mu_B$ in **4** and **4a**, respectively (see Figures 4a and 4b). This behaviour

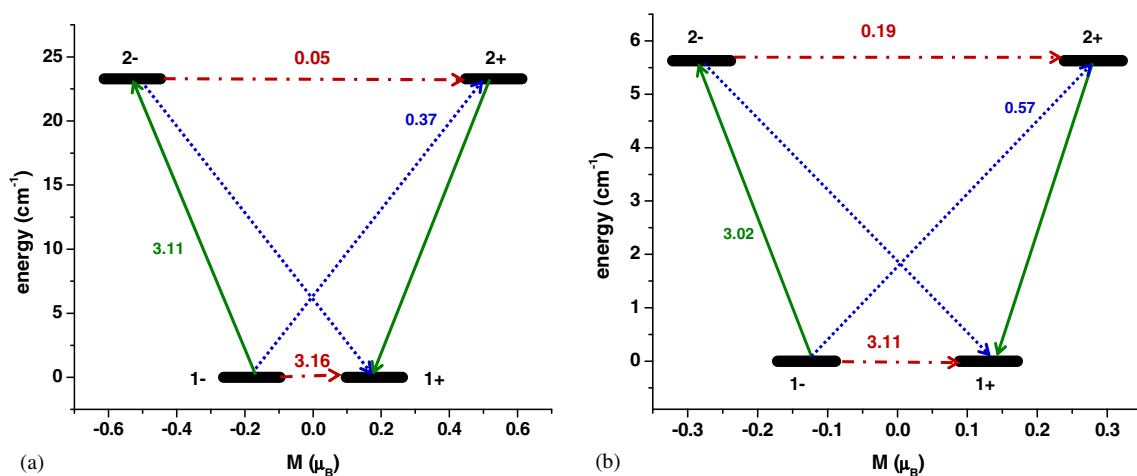


Figure 4. *Ab initio* calculated magnetization blocking barrier for complexes; (a) **4** and (b) **4a**. The thick black line represents the Kramers doublets (KDs), as a function of magnetic moment. The blue dotted lines indicate the possible path for the Orbach process. The solid green arrows imply the most probable relaxation pathways for magnetization reversal. The dashed-dotted red lines correspond to the presence of QTM/TA-QTM between the connecting pairs. The numbers at each arrow are the mean absolute value for the corresponding matrix element of transition magnetic moment.

facilitates efficient QTM within the ground state precluding zero-field SIM behaviour in both of these complexes. However, on application of magnetic field, analysis of first excited KD becomes imperative. In complexes **4** and **4a**, even the first excited state is also associated with significant transverse components with very small value of g_z (3.17 and 2.14 for **4** and **4a**, respectively). This indicates relaxation *via* this level with U_{cal} value of 23.3 and 5.6 cm^{-1} for **4** and **4a** (Table 1), respectively. Such small value of barrier in complex **4a** supports experimental absence of SIM behaviour nicely. Though for complex **4**, the first excited level energy is comparable to that of complex **2a**, significant g_x/g_y component in conjunction with small g_z component completely destroys the SIM behaviour even in the presence of applied dc magnetic field. Ground state axial crystal field parameters are marginally larger ($B_2^0 = 1.37$ and 1.26 for **4** and **4a**, respectively) than corresponding non-axial terms ($B_2^{-1,+1}$) and are of competing magnitude (see Table S9 in SI). This suggests probability of QTM within ground state for both the complexes reiterating our earlier statements. For both the compounds, g_z orientation intersects through the negatively charged three ligands in order to encounter least electrostatic repulsion (Figures 1g and 1h). Our computed data is further substantiated by nice agreement between calculated and experimental $\chi_{\text{m}}T$ vs T plots (Figures 3g and 3h).

3.5 Comparative analysis of single-ion anisotropy behaviour of complexes **1–4** and **1a–4a**

Our calculations reproduce the experimental SIM behaviour for complexes **1** ($U_{\text{cal}} = 256.36 \text{ cm}^{-1}$) and **2** ($U_{\text{cal}} = 268.50 \text{ cm}^{-1}$). On the other hand, though computations predicted large energy barrier for magnetization reorientation for complex **1a** ($U_{\text{cal}} = 229.39 \text{ cm}^{-1}$), experimentally only high frequency tail (χ'') was detected at 1250 Oe magnetic field with U_{eff} of 21 cm^{-1} . Calculated lower U_{cal} value for complex **2a** ($U_{\text{cal}} = 23.19 \text{ cm}^{-1}$) was in line with experimental high frequency tails (χ'') at 1250 Oe. Rest of the four complexes containing Ho^{III} (**3** and **3a**) and Er^{III} (**4** and **4a**) ions lack SIM behaviour. Complexes with non-Kramers ion are found to be superior in producing larger barrier height for magnetization reversal. Axial alignment of the N-heterocyclic carbene as well as bis(pyrazolyl)borate ligand around Ln^{III} ions is favourable for ions with oblate 4f electron density (Tb^{III} , Dy^{III} and Ho^{III}) while unfavourable for Er^{III} ion with prolate electron density. Though Dy^{III} and Er^{III} ions possess similar m_j value of 15/2, they differ in the shape of 4f electron density. This is evident through the stabilisation of $m_j = \pm 15/2$ and 1/2 ground state

KD for complexes **2/2a** and **4/4a**, respectively. This can be ascribed to the unfavourable axial ligand position around Er^{III} resulting in removal of SIM characteristics. N-heterocyclic carbene compounds are axially compressed trigonal prismatic structure as compared to that constituted by bis(pyrazolyl)borate ligand. This leads to comparatively better SIM characteristics for the N-heterocyclic-carbene analogues as compared to their corresponding bis(pyrazolyl)borate ligand analogues for all the complexes. Between complexes **2** and **2a**, observation of prominent transverse anisotropic components in later complex is affirmative of stronger crystal field mixing of the free-ion states in **2a**. On the other hand, stronger crystal field mixing of the free-ion states and resultant poorly defined energy multiplets in complex **4a** as compared to **4** has been manifested by distinctive deviation between ground and first excited anisotropy direction (0.7° vs 8.3° for **4** vs **4a**). Besides, it is notable that, larger deviation of first excited anisotropic direction with respect to the ground state is suggestive of low-symmetry ligand field environment. Hence, U_{cal} value varies as complex **1** \approx **2** $>$ **1a** $>$ **2a**, revealing better behaviour for carbene analogues. For complexes **1/1a**, $m_j = \pm 6$ has been stabilised as ground state in accordance with the expectation. However, for **3/3a**, $m_j = \pm 7$ has been stabilised as ground pseudo-doublet in contrary to the expected stabilisation of $m_j = \pm 8$ pseudo-doublet. This clearly demonstrates the comparatively lower symmetry ligand environment for Ho^{III} -based complexes as compared to their Tb^{III} analogues. This was further corroborated by first excited tunnelling gap for 0.03 vs 3.04 cm^{-1} for **1** vs **3** and 0.04 vs 12.35 cm^{-1} for **1a** vs **3a**. Even within the similar ion analogues, tunnel splitting of first excited pseudo-doublet in pyrazole-ligated complex **1a/3a** is much larger than that in complex **1/3** (carbene ligated) reiterating our earlier statement of better SIM behaviour for carbene analogues. Hence, despite the lower energy magnitude of first excited pseudo-doublet for **3** (9.01 cm^{-1}) in comparison with **3a** (13.08 cm^{-1}), tunnel splitting dictates the magnetic behaviour and larger Δ_{tun} for **3a** indicates poor SIM characteristics for **3a**. Thus, our calculations based on U_{cal} value predict the following trend: **1** \approx **2** $>$ **1a** $>$ **4** $>$ **2a** $>$ **3a** $>$ **3** $>$ **4a**. The magnetic analysis of all the eight complexes are summarized in Table 2.

3.6 Role of Ln-L Bonding in influencing Magnetic Anisotropy of complexes **1–4** and **1a–4a**

3.6a Charge and Spin Density Analysis: To understand the role of CF parameters and the 4f-ligand interactions, we have analysed the charges and the spin

Table 2. Comparative magnetic analysis on eight complexes studied.

Complexes	U_{eff} (cm^{-1})	U_{cal} (cm^{-1})	Experimental relaxation metrics	Calculated relaxation metrics
1	44.8(45.2)	256.36	–	Via 1 st excited KD $\Delta_{\text{tun}} = 0.02$ and 0.03 cm^{-1} for ground and first excited pseudo-doublet, respectively
2	32.8(33.6)	268.50*	QTM=3.1	Via 4 th excited KD QTM=0.03, 0.03, 0.03, 0.05 and $1.76 \mu_{\text{B}}$, respectively for ground, 1 st , 2 nd , 3 rd , 4 th , 5 th KD
3	–	9.01	–	Via 1 st excited KD $\Delta_{\text{tun}} = 0.04$ and 3.04 cm^{-1} for ground and first excited pseudo-doublet, respectively
4	–	23.29	–	Via 1 st excited KD QTM=3.16 and $0.05 \mu_{\text{B}}$, respectively, for ground and 1 st excited KD
1a	21	229.39	QTM=115.9	Via 1 st excited KD $\Delta_{\text{tun}} = 0.05$ and 0.04 cm^{-1} for ground and first excited pseudo-doublet, respectively
2a	–	23.19	–	Via 1 st excited KD QTM=0.02 and $0.10 \mu_{\text{B}}$, respectively, for ground and 1 st excited KD
3a	–	13.08	–	Via 1 st excited KD $\Delta_{\text{tun}} = 0.07$ and 12.35 cm^{-1} for ground and first excited pseudo-doublet, respectively
4a	–	5.63	–	Via 1 st excited KD QTM=3.11 and $0.19 \mu_{\text{B}}$, respectively, for ground and 1 st excited KD

densities obtained from DFT calculations. In all the complexes, metal ions possess positive spin density while the six-coordinated C (for complexes **1**, **2**, **3**, **4**) and N (for complexes **1a**, **2a**, **3a**, **4a**) atoms show small negative spin density. This clearly reveals mixture of spin delocalization and polarization with preponderant spin polarization on the coordinated ligand donor atoms (Figure 5). Mulliken charge analysis predicts strong crystal field around the carbene ligated complexes as compared to their pyrazole analogues. This can be attributed to the negative charges on the C atoms of carbene ligands while positive charges were computed on the ligated nitrogen atoms of the pyrazole ligands (see Table 3 and for corresponding atomic numbers see Figure S2 in Supplementary Information). In order to gain insights into the orientation of principal anisotropy axis (g_z), we have also performed analysis based on simple electrostatic model.⁹⁸ The calculated orientations of the magnetic moments of the ground state for **2** and **2a** (Figure S1 in SI) resemble the alignment expected from *ab initio* calculations (deviation between *ab initio* and electrostatic anisotropic axis is 0.23° and 0.48° for **2** and **2a**, respectively).

3.6b NBO Analysis: To gain clues into the nature of Ln-L bonding, NBO calculations were also carried out

on all the eight complexes to understand the Ln—H-B interactions. For all the complexes, we have focussed on the charge transfer interaction between B-H bond moiety and metal ion. On this note, we have computed charge transfer interaction stabilization energy from the donor $\sigma_{\text{B-H}}$ bond to the acceptor p-d hybrid orbital of the Ln^{III} ions. In all the complexes, NBO second order perturbation analysis reveals larger stabilization energy for the donor B-H bond to acceptor Ln^{III} ions in the corresponding pyrazole ligated complexes as compared to their corresponding carbene analogues (see Figures S3–S18 in SI). This can be attributed to the larger bite angle, smaller Ln—H distance of the pyrazole analogues. The Wiberg bond indexes computed for the Dy^{III}—H in **2** and **2a** are 0.01 and 0.02, respectively. This suggests the presence of stronger agostic interaction in pyrazole analogues compared to the carbene analogues (see section 3.6c). A similar trend was evident for all the carbene and pyrazole analogues of the three other metal ions (Tb^{III}, Ho^{III} and Er^{III}). The NBO analysis for **2** reiterates the nature of B-H bonding between the two sites where B-H is found to be strongly covalent possessing a significant σ character with 45.91. Similarly, for **2a** as well, 45.59 calculated for the B-H bond implying its σ -character. For all other six complexes, 45 corresponding B-H bonds.

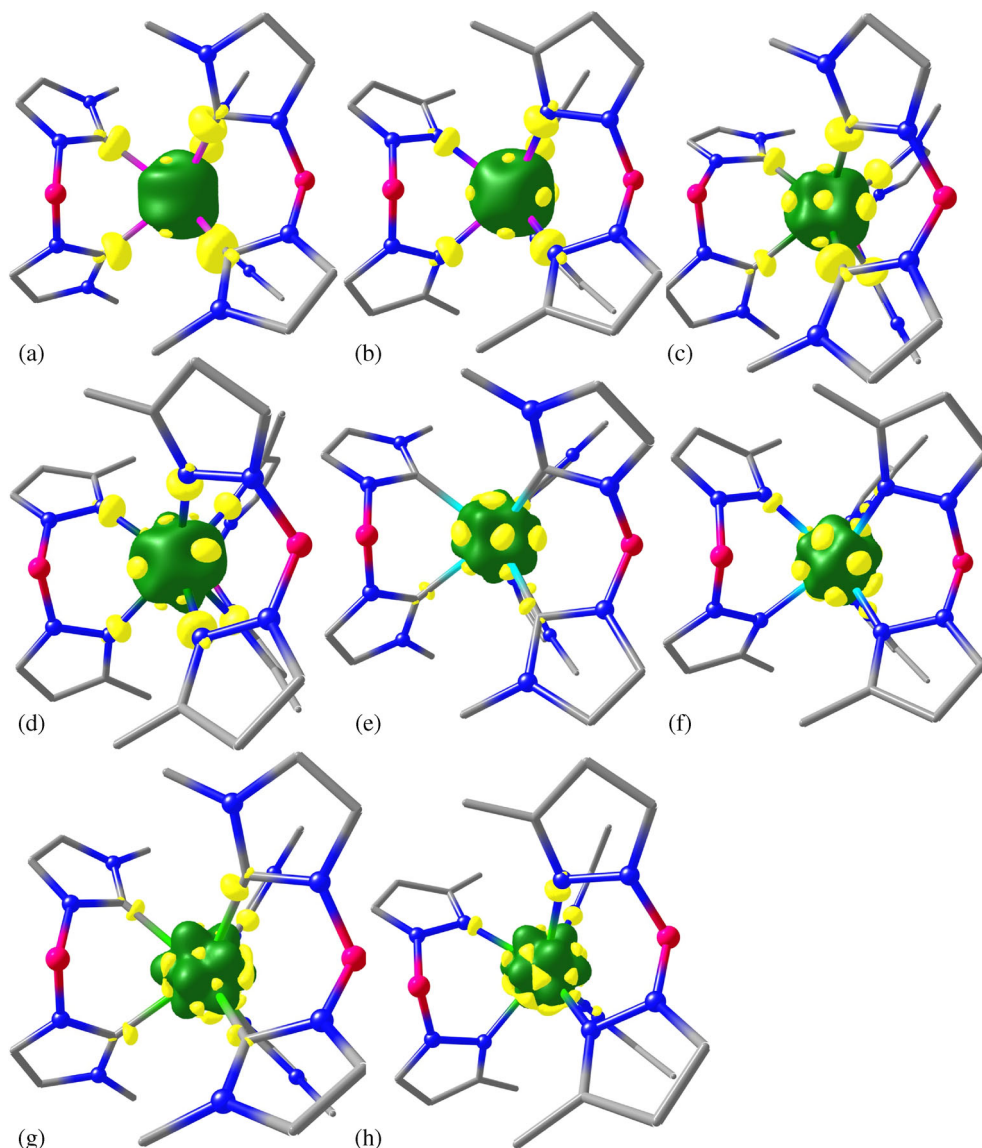


Figure 5. DFT-computed spin density plots for complexes; (a) **1**, (b) **1a**, (c) **2**, (d) **2a**, (e) **3**, (f) **3a**, (g) **4** and (h) **4a**. The isodensity surface represented corresponds to a value of $0.0009 \text{ e}^-/\text{bohr}^3$. The green and yellow regions correspond to positive and negative spin densities, respectively.

3.6c QTAIM Analysis: We have investigated the topological properties at the bond critical point (BCPs) for the chosen complexes. All the systems analyzed here clearly display BCPs indicating the bonded and the non-bonded interactions that exist in the complexes. In the molecular graph (Figure S1 in SI), the big circles correspond to attractors attributed to positions of atoms and critical points such as $(3, -1)$ BCP (red), $(3, +1)$ RCP (yellow) and $(3, +3)$ CCP (green) indicated by small circles.

The topological properties at BCPs for Ln-C(N) and Ln \cdots H–BH is collected in Tables 4 and 5 (complete topological properties are given in Tables S10 and S11 in Supporting Information) respectively. The lanthanide

(Ln) atom forms six bonds with each C/N atom of the three ligand (*via* C or N). It is seen that in all the complexes, there are mainly two different bond paths have been observed between Ln and ligand. Among them, six interactions are Ln \cdots C(N) type and remaining three are Ln \cdots H–BH type agostic interactions (refer Figure S19 in SI). In addition to this several other interactions also present.

The electron density $\rho(r)$ at the BCP between Ln and the C1/N1 atoms of **1–4** and **1a–4a** shows values of 0.0467, 0.0458, 0.0478, 0.0351 and 0.0458, 0.0477, 0.0454 and 0.0623 au, respectively. It is seen that $\rho(r)$ is small ($0.0363 \text{ au} < \rho(r) < 0.0986 \text{ au}$) and $\nabla^2_{\rho(r)}$ is small positive ($0.0277 \text{ au} < \nabla^2_{\rho(r)} < 0.16642 \text{ au}$), indicating

Table 3. DFT-computed Mulliken charges for complexes **1–4** and **1a–4a**, where the atomic number of respective complexes have been taken from pictorial representation (Figure S2 in Supplementary Information) of the core structure containing metals with six-coordination number ligated donor atoms.

Complex 1	Mulliken charge	Complex 1a	Mulliken charge	Complex 2	Mulliken charge	Complex 2a	Mulliken charge
Tb ^{III}	0.84	Tb ^{III}	1.59	Dy ^{III}	0.86	Dy ^{III}	1.62
C1	−0.19	N1	0.07	C1	−0.19	N1	0.06
C2	−0.23	N2	0.06	C2	−0.24	N2	0.07
C3	−0.19	N3	0.07	C3	−0.19	N3	0.06
C4	−0.24	N4	0.07	C4	−0.24	N4	0.07
C5	−0.19	N5	0.06	C5	−0.19	N5	0.06
C6	−0.24	N6	0.06	C6	−0.24	N6	0.07
Complex 3	Mulliken charge	Complex 3a	Mulliken charge	Complex 4	Mulliken charge	Complex 4a	Mulliken charge
Ho ^{III}	0.55	Ho ^{III}	1.43	C1	−0.19	N1	0.05
C1	−0.20	N1	0.10	C2	−0.23	N2	0.08
C2	−0.14	N2	0.08	Er ^{III}	0.80	Er ^{III}	1.55
C3	−0.20	N3	0.10	C4	−0.24	N3	0.05
C4	−0.14	N4	0.09	C5	−0.18	N4	0.08
C5	−0.20	N5	0.10	C6	−0.24	N5	0.05
C6	−0.14	N6	0.08	C3	−0.18	N6	0.08

Table 4. Topological parameters at BCPs in the Ln–C(N) bonds of the complexes **1–4** and **1a–4a**. $\rho(r)$ in units of eÅ^{−3}.

Complexes	Ln–C1(N1) bonds		Ln–C2(N2) bonds		Ln–C3(N3) bonds		Ln–C4(N4) bonds		Ln–C5(N5) bonds		Ln–C6(N6) bonds	
	$\rho(r)$	$\nabla^2_{\rho(r)}$										
1	0.0467	0.0277	0.0475	0.0279	0.0471	0.0280	0.0476	0.0288	0.0470	0.0281	0.0363	0.0297
2	0.0458	0.0259	0.0470	0.0265	0.0459	0.0263	0.0471	0.0266	0.0455	0.0277	0.0466	0.0278
3	0.0478	0.0296	0.0467	0.0291	0.0479	0.0310	0.0466	0.0293	0.0478	0.0299	0.0465	0.0289
4	0.0351	0.0730	0.0853	0.1030	0.0368	0.0750	0.0859	0.1099	0.0299	0.0527	0.0816	0.1001
1a	0.0458	0.0382	0.0467	0.0394	0.0458	0.0382	0.0467	0.0393	0.0456	0.0384	0.0466	0.0400
2a	0.0477	0.0375	0.0466	0.0373	0.0477	0.0381	0.0469	0.0372	0.0476	0.0373	0.0465	0.0367
3a	0.0454	0.0398	0.0467	0.0415	0.0459	0.0398	0.0470	0.0412	0.0451	0.0397	0.0467	0.0407
4a	0.0623	0.1007	0.0986	0.1641	0.0906	0.1463	0.0920	0.1642	0.1010	0.1629	0.0962	0.1664

Table 5. Topological parameters at BCPs in the Ln⋯H–BH bonds of the complexes **1–4** and **1a–4a**. $\rho(r)$ in units of eÅ^{−3}.

Complexes	Ln⋯H1–BH		Ln⋯H2–BH		Ln⋯H3–BH	
	$\rho(r)$	$\nabla^2_{\rho(r)}$	$\rho(r)$	$\nabla^2_{\rho(r)}$	$\rho(r)$	$\nabla^2_{\rho(r)}$
1	0.0112	0.0115	0.0112	0.0113	0.0112	0.0115
2	0.0106	0.0105	0.0107	0.1056	0.0106	0.0105
3	0.0114	0.0120	0.0114	0.0121	0.0114	0.0118
4	0.0031	0.0043	0.0323	0.0040	0.0334	0.0154
1a	0.0209	0.0184	0.0208	0.0180	0.0208	0.0183
2a	0.0192	0.0158	0.0193	0.0158	0.0193	0.0158
3a	0.0198	0.0191	0.0202	0.0187	0.0199	0.0192
4a	0.0563	0.0552	0.0543	0.0630	0.0529	0.0638

a “closed” shell character of the coordination bonds.⁹⁹ The electron density $\rho(r)$ at the BCP between Ln and other carbon atoms (C2, C3, C4, C5 and C6) follows the same trend. The partly covalent nature of investigated interactions can then be supported by values of

$|V(r)|/G(r)$ ratio.^{99,100} $|V(r)|/G(r) < 1$ is characteristic of a typical ionic interaction and $|V(r)|/G(r) > 2$ is diagnostic of a ‘classical’ covalent interaction. Taking all these criteria into consideration, the QTAIM-defined topological properties at BCPs indicate a mixed (largely

ionic with significant covalent component) character of these coordination bonds, also because $|V(r)|/G(r) < \sim 1.16$ condition has been met in all cases. The Laplacian function $\nabla_{\rho(r)}^2$ at the BCP between Ln and the C1/N1 atoms of **1–4** and **1a–4a** shows values of 0.00277, 0.0259, 0.0296, 0.0730 and 0.0382, 0.0375, 0.0398 and 0.1007 au for Tb, Dy, Ho and Er, respectively. All other Ln-C and Ln-N bonds also shows similar values Laplacian function $\nabla_{\rho(r)}^2$. Based on QTAIM analysis, it is interesting to note that the pyrazole ligated Ln-C bonds (**1a–4a**) are stronger as compared to carbene ligated complexes (**1–4**).

Figure 6 shows comparative plots of the negative Laplacian function $\nabla_{\rho(r)}^2$ through Ln-C and Ln-N plane for complex **2** and **2a**. It is evident that the valence shell charge concentration (VSCC) zone of the carbenic carbon atom is more diffused towards the group Dy atom in complex **2** (Figure 6) than in complex **2a**. This indicates that there is a larger charge transfer from the carbenic C atom to the Dy atom than N atom. The calculated topological properties at the BCP between the interacting atoms with the corresponding ligand suggest that as the

size of the atom increases, the charge density at BCP decreases.

To ascertain the nature of the interaction between the H–BH and Ln, AIM analysis was performed. In all the cases, the $\rho(r)$ values are 0.0112 to 0.0209 au which indicates a weak interaction as expected. In addition, all the interactions investigated in the Ln \cdots H BCPs are characterized by positive values of $\rho(r)$ and $\nabla_{\rho(r)}^2$ which suggest that it should be considered as closed-shell interactions of agostic type. The $|V(r)|/G(r) < 1.0$ is also met, indicating partly covalent Ln \cdots BH interactions for all the complexes. The QTAIM results show that the agostic bonds are characterized by Ln \cdots H–BH bond paths that are straight in the Ln \cdots BCP section and highly curved near the agostic hydrogen (refer Figure S19 in SI). The ellipticity (ϵ) computed at Ln \cdots H–BH BCP has greater values, which also confirms the presence of agostic interaction. This agrees well with the earlier reports.^{101–104} It is important to note that BCP is significantly closer to the agostic hydrogen in complexes with Ln \cdots H–BH agostic bonds (Figure 7).

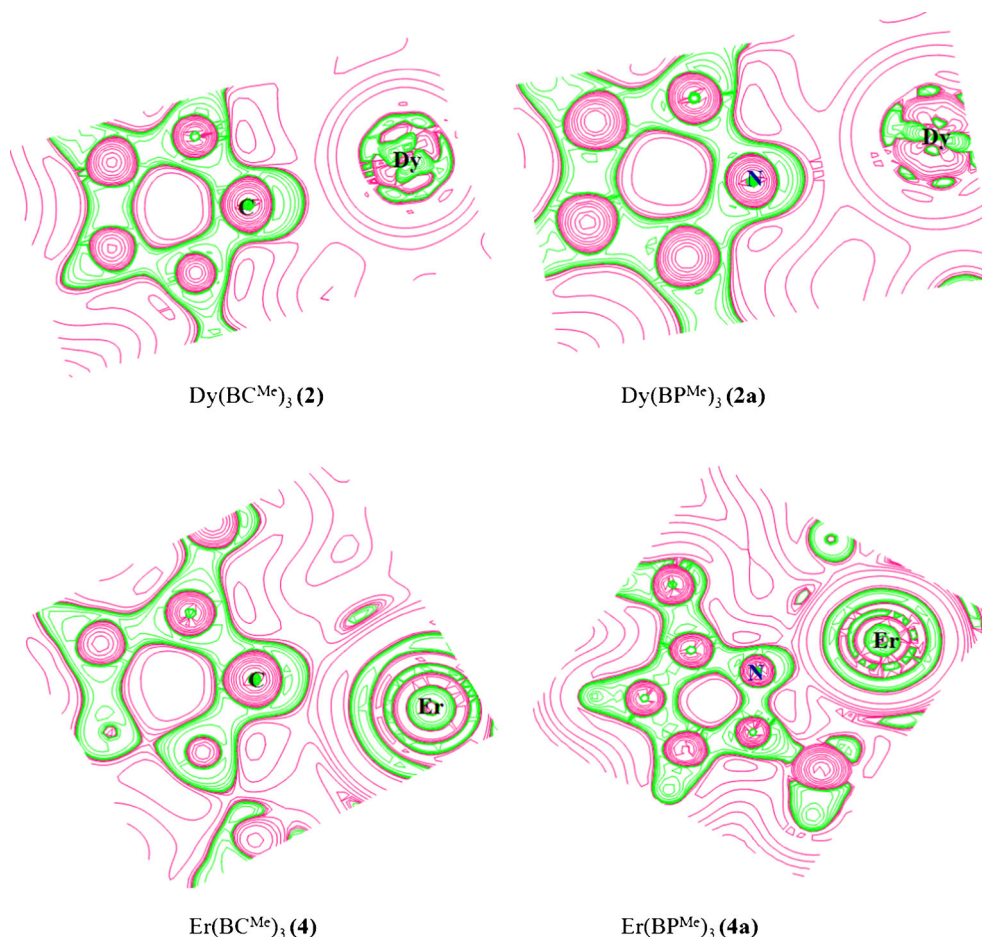


Figure 6. Contour line diagram of the Laplacian of electron density along the Ln–C/Ln–N plane in complexes **2**, **2a** and **4**, **4a**.

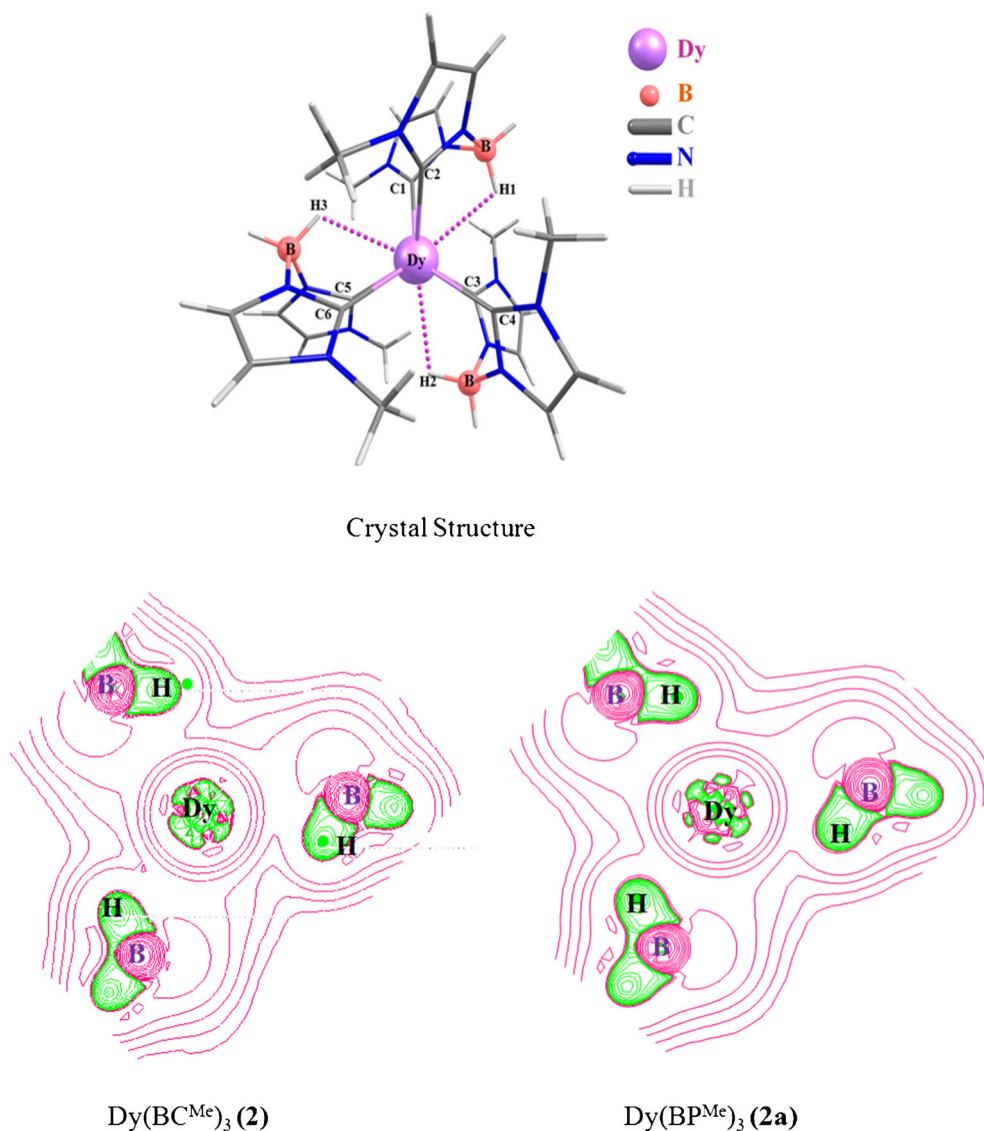


Figure 7. Top - Crystal structure showing agostic interactions. Bottom - Contour line diagram of the Laplacian of electron density along the three agostic Ln^{III}H–BH interactions (drawn on the agostic plane) in Dy(BCMe)₃ (**2**) and Dy(BCMe)₃ (**2a**).

In all the complexes, the three Ln^{III}H–BH interactions make the tricapped trigonal prismatic geometry around the metal centre. The Lanthanide atoms make bonds with the three ligands *via* six carbon (C1–C2, C3–C4 and C5–C6) and six nitrogen atoms (N1–N2, N2–N4 and N5–N6) for **1–4** and **1a–4a**, respectively. Among them C1, C3, C5 (N1, N3, N5) and C2, C4, C6 (N2, N4, N6) make triangles. The *ab initio* results show that, the main anisotropic g-tensor is oriented perpendicular to the Ln^{III}H–BH interactions and centre of the C1, C3, C5 (N1, N3, N5) triangle. This is due to the presence of three Ln^{III}H–BH interactions and the C1, C3, C5 (N1, N3, N5) triangle. The Laplacian of electron density drawn along the three carbon (C–C–C) plane in **2** and **2a** shows less charge concentration in the triangle 1 (Figure S20 in SI).

To probe and quantify the prolate and oblate nature of the electron density the comparative plots of the negative Laplacian function $\nabla_{\rho(r)}^2$ through Ln–C and Ln–N plane has been analysed. The Laplacian function $\nabla_{\rho(r)}^2$ value against this general prolate-oblate classification is plotted in Figure 8. Quite interestingly, the Laplacian function $\nabla_{\rho(r)}^2$ was found to quantify the qualitative oblate-prolate nature of the electron density with values larger than 0.07 au describing prolate shape and smaller values classified as oblate. Within the oblate set studied, the Tb is found to possess stronger oblate character followed by Dy and Ho. This is strikingly matching with the expectation based on the popular qualitative analysis,⁵⁰ except for the fact that Laplacian function $\nabla_{\rho(r)}^2$ explicitly quantify them based on the ligand field employed. The same is also visible

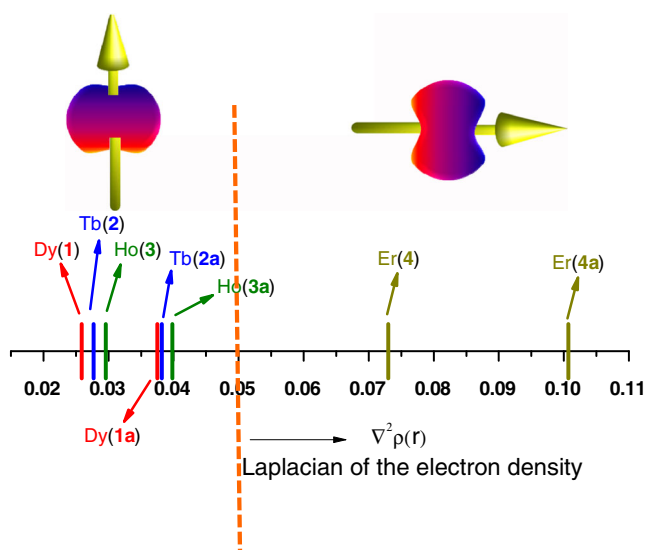


Figure 8. The Laplacian function $\nabla^2_{\rho(r)}$ value plotted against general prolate-oblate classification.

when the Laplacian function $\nabla^2_{\rho(r)}$ is plotted at the Ln-L plane.

4. Conclusions

To summarise, we have undertaken a detailed *ab initio* and DFT, QTAIM calculations on a series of lanthanide $M(\text{Bc}^{\text{Me}})_3$ ($M = \text{Tb}$ (**1**), Dy (**2**), Ho (**3**), Er (**4**), $[\text{Bc}^{\text{Me}}]^-$ = dihydrobis(methylimidazolyl)borate) and $M(\text{Bp}^{\text{Me}})_3$ ($M = \text{Tb}$ (**1a**), Dy (**2a**), Ho (**3a**), Er (**4a**) $[\text{Bp}^{\text{Me}}]^-$ = dihydrobis(methylpyrazolyl)borate) complexes to shed light on the magnetic properties and to probe how lanthanide-ligand bonding influences the magnetic properties. Conclusions drawn from our work are summarized below:

1. Our calculations reproduced experimental absence/presence of SIM characteristic for all the eight studied complexes nicely (except complex **1a**). Among all the eight complexes studied, only complexes **1** and **2** show SIM behaviour with $U_{\text{cal}}/U_{\text{eff}}$ values of 256.4/45.2 and 268.5/33.6 cm^{-1} for **1** and **2**, respectively.
2. Experimentally, though complex **1a** only shows variable field frequency dependent χ'' tails ($U_{\text{eff}} = 21 \text{ cm}^{-1}$), our calculations reveal much larger energy barrier of 229.4 cm^{-1} contrary to experiment. Small computed barrier height for complex **2a** (23.2 cm^{-1}) justifies the experimentally observed frequency dependent χ'' tails. Rest of the four complexes (**3**, **4**, **3a** and **4a**) lack SIM characteristics. Hence, in this set of complexes, Tb^{III} ($4f^8$) and Dy^{III} ($4f^9$) ions are found to instil improved SIM

behaviour as compared to Ho^{III} ($4f^{10}$)/ Er^{III} ($4f^{11}$) ions.

3. Correlation between ligand field environment and nature of 4f electron density has been corroborated by our calculations. Axial positioning of the ligand (N-heterocyclic carbene or bis(pyrazolyl) borate) has favoured stabilisation of energy multiplet with larger angular momentum projection; *i.e.*, $\pm m_j = 15/2$, **2a** and **3a** for Dy^{III} , Tb^{III} and Ho^{III} ions with 4f oblate electron density respectively. However, in Er^{III} compounds (prolate 4f electron density), lowest angular momentum multiplet was computed to be the ground state ($\pm m_j = 1/2$) as such metal ions necessitate presence of equatorial crystal field.
4. Calculations yield the following trend in the U_{cal} values: **1** \approx **2** $>$ **1a** $>$ **4** $>$ **2a** $>$ **3a** $>$ **3** $>$ **4a** and this is consistent with the experimental observations. We have also attempted to ascertain the location of anisotropy orientation which pierces out amidst the six coordinated ligand donor atoms of the three coordinating ligands in order to minimise electrostatic repulsion.
5. DFT-computed Mulliken charge analysis clearly revealed larger negative charges on the coordinated C-atoms of carbene ligand while small positive charge was detected on coordinated N-atoms of the pyrazole ligand. This essentially leads to stronger crystal field environment for carbene analogues. NBO and Wiberg bond index analysis also reaffirmed the presence of stronger $\text{Ln}^{\text{III}}\text{H}-\text{B}$ agostic interaction for the pyrazole analogues as compared to their carbene analogues.
6. QTAIM analysis provides evidence for a direct interaction between the agostic hydrogen atom and the metal, *viz.*, smaller $\rho(r)$ values at the $\text{Ln}^{\text{III}}\text{H}-\text{BH}$, larger ε of the $\text{Ln}^{\text{III}}\text{H}-\text{BH}$ BCPs. Most importantly, the Laplacian function $\nabla^2_{\rho(r)}$ was found to quantify the qualitative oblate-prolate nature of the electron density explicitly based on the ligand field employed and this is likely to have influence beyond the example presented.

Supplementary Information (SI)

We have summarised the energies (cm^{-1}), corresponding g-tensors, tunnel splitting (cm^{-1}), crystal field parameters and angle between main magnetic axis of ground state energy multiplet and higher excited levels of all the Kramers doublets and pseudo-doublets in **2**, **2a**, **4**, **4a** and **1**, **1a**, **3**, **3a**, respectively, in Tables S1–S9. The orientation of the principal anisotropy axis (gz) for complexes a) **2** and b) **2a** are given in Figure S1. The

core structural moieties of complexes atom numbers correspond to the representation of Mulliken charges are given in the Figure S2. The second-order perturbation theory computed donor-acceptor charge transfer stabilisation energy in all the eight complexes are given in Figures S3–S18. The molecular graphs of the complexes and the contour line diagram of the Laplacian of electron density drawn along the three carbon (C-C-C) plane are given in the Figures S19 and S20 respectively.

Acknowledgements

GR would like to thank SERB (EMR/2014/00024) for the funding. TG would like to thank UGC New Delhi for SRF fellowship. GV would like to thank Indian Institute of Technology Bombay for Post-Doctoral fellowship.

References

1. Wang H, Wang B-W, Bian Y, Gao S and Jiang J 2016 *Coord. Chem. Rev.* **306** 195
2. Liddle S T and van Slageren J 2015 *Chem. Soc. Rev.* **44** 6655
3. Feltham H L C and Brooker S 2014 *Coord. Chem. Rev.* **276** 1
4. Woodruff D N, Winpenny R E P and Layfield R A 2013 *Chem. Rev.* **113** 5110
5. Wang B W, Wang X Y, Sun H L, Jiang S D and Gao S 2013 *Philos. Trans. R. Soc. London, Ser. A* **371** 20120316
6. Habib F and Murugesu M 2013 *Chem. Soc. Rev.* **42** 3278
7. Sorace L, Benelli C and Gatteschi D 2011 *Chem. Soc. Rev.* **40** 3092
8. Friedman J R and Sarachik M P 2010 *Annu. Rev. Condens. Matter Phys.* **1** 109
9. Luzon J and Sessoli R 2012 *Dalton Trans.* **41** 13556
10. Wang B, Jiang S, Wang X and Gao S 2009 *Sci. China, Ser. B Chem.* **52** 1739
11. Sessoli R and Powell A K 2009 *Coord. Chem. Rev.* **253** 2328
12. Ishikawa N 2007 *Polyhedron* **26** 2147
13. Pedersen K S, Bendix J and Clerac R 2014 *Chem. Commun.* **50** 4396
14. Saitoh E, Miyajima H, Yamaoka T and Tataru G 2004 *Nature* **432** 203
15. Leuenberger M N and Loss D 2001 *Nature* **410** 789
16. Yamanouchi M, Chiba D, Matsukura F and Ohno H 2004 *Nature* **428** 539
17. Bogani L and Wernsdorfer W 2008 *Nat. Mater.* **7** 179
18. Xiong G, Qin X Y, Shi P F, Hou Y L, Cui J Z and Zhao B 2014 *Chem. Commun.* **50** 4255
19. Li D P, Wang T W, Li C H, Liu D S, Li Y Z and You X Z 2010 *Chem. Commun.* **46** 2929
20. Baldoví J J, Cardona-Serra S, Clemente-Juan J M, Coronado E, Gaita-Ariño A and Palií A 2012 *Inorg. Chem.* **51** 12565
21. Meihaus K R and Long J R 2013 *J. Am. Chem. Soc.* **135** 17952
22. Chen G J, Guo Y N, Tian J L, Tang J, Gu W, Liu X, Yan S P, Cheng P and Liao D Z 2012 *Chem. Eur. J.* **18** 2484
23. Ungur L, Le Roy J J, Korobkov I, Murugesu M and Chibotaru L F 2014 *Angew. Chem. Int. Ed.* **53** 4413
24. Clemente-Juan J M, Coronado E and Gaita-Ariño A 2015 In *Lanthanides and Actinides in Molecular Magnetism* (Weinheim: Wiley-VCH Verlag) pp. 27–60
25. Jiang S-D, Wang B-W and Gao S 2014 (Berlin Heidelberg: Springer) pp. 1–31
26. Ganivet C R, Ballesteros B, de la Torre G, Clemente-Juan J M, Coronado E and Torres T 2013 *Chem. Eur. J.* **19** 1457
27. Sun W-B, Yan P-F, Jiang S-D, Wang B-W and Zhang Y-Q 2016 *Chem. Sci.* **7** 684
28. Jeletic M, Lin P H, Le Roy J J, Korobkov I, Gorelsky S I and Murugesu M 2011 *J. Am. Chem. Soc.* **133** 19286
29. Ishikawa N, Sugita M, Ishikawa T, Koshihara S and Kaizu Y 2003 *J. Am. Chem. Soc.* **125** 8694
30. Aromi G and Brechin E K 2006 *Struct. Bond.* **122** 1
31. Ishikawa N, Sugita M, Ishikawa T, Koshihara S and Kaizu Y 2004 *J. Phys. Chem. B* **108** 11265
32. Gregson M, Chilton N F, Ariciu A-M, Tuna F and Crowe I F 2016 *Chem. Sci.* **7** 155
33. Chilton N F, Langley S K, Moubaraki B, Soncini A, Batten S R and Murray K S 2013 *Chem. Sci.* **4** 1719
34. Boulon M E, Cucinotta G, Luzon J, Degl'Innocenti C and Perfetti M 2013 *Angew. Chem. Int. Ed.* **52** 350
35. Chilton N F 2015 *Inorg. Chem.* **54** 2097
36. Chilton N F, Goodwin C A P, Mills D P and Winpenny R E P 2015 *Chem. Commun.* **51** 101
37. Blackburn O A, Chilton N F, Keller K, Tait C E and Myers W K 2015 *Angew. Chem. Int. Ed.* **54** 10783
38. Mei X-L, Ma Y, Li L-C and Liao D-Z 2012 *Dalton Trans.* **41** 505
39. Gatteschi D and Sorace L 2001 *J. Solid State Chem.* **159** 253
40. Rechkemmer Y, Fischer J E, Marx R, Dörfel M and Neugebauer P 2015 *J. Am. Chem. Soc.* **137** 13114
41. Chen Y-C, Liu J-L, Ungur L, Liu J and Li Q-W 2016 *J. Am. Chem. Soc.* **138** 2829
42. Goswami T and Misra A 2012 *J. Phys. Chem. A* **116** 5207
43. Pedersen K S, Ungur L, Sigrist M, Sundt A and Schau-Magnussen M 2014 *Chem. Sci.* **5** 1650
44. Oyarzabal I, Ruiz J, Ruiz E, Aravena D and J M Seco 2015 and, Colacio E *Chem. Commun.* **51** 12353
45. Chen G-J, Gao C-Y, Tian J-L, Tang J and Gu W 2011 *Dalton Trans.* **40** 5579
46. Mondal A K, Goswami S and Konar S 2015 *Dalton Trans.* **44** 5086
47. Wang Y-L, Gu B, Ma Y, Xing C and Wang Q-L 2014 *CrystEngComm* **16** 2283
48. Pugh T, Tuna F, Ungur L, Collison D and McInnes E J L 2015 *Nat. Commun.* **6** 7492
49. Das S, Bejoymohandas K S, Dey A, Biswas S, Reddy M L P and et al. 2015 *Chem. Eur. J.* **21** 6449
50. Rinehart J D and Long J R 2011 *Chem. Sci.* **2** 2078
51. Gudel H U, Hauser U and Furrer A 1979 *Inorg. Chem.* **18** 2730

52. Amoretti G, Caciuffo R, Carretta S, Guidi T, Magnani N and Santini P 2008 *Inorg. Chim. Acta* **361** 3771
53. Bencini A and Gatteschi D 1990 In *EPR of Exchange Coupled Systems* (Berlin: Springer-Verlag)
54. Barra A L, Gatteschi D, Sessoli R, Abbati G L and Cornia A 1997 *Angew. Chem. Int. Ed.* **36** 2329
55. Liu J, Chen Y-C, Jia J-H, Liu J-L and Vieru V 2016 *J. Am. Chem. Soc.* **138** 5441
56. Ungur L and Chibotaru L F 2015 In *Lanthanides and Actinides in Molecular Magnetism* (Weinheim: Wiley-VCH Verlag) pp. 153–184
57. Huang X-C, Vieru V, Chibotaru L F, Wernsdorfer W, Jiang S-D and Wang X-Y 2015 *Chem. Commun.* **51** 10373
58. Marx R, Moro F, Dorfel M, Ungur L and Waters M 2014 *Chem. Sci.* **5** 3287
59. Le Roy J J, Ungur L, Korobkov I, Chibotaru L F and Murugesu M 2014 *J. Am. Chem. Soc.* **136** 8003
60. Guo Y-N, Ungur L, Granroth G E, Powell A K and Wu C 2014 *Sci. Rep.* **4** 5471
61. Chibotaru L F 2014 In *Theoretical Understanding of Anisotropy in Molecular Nanomagnets* (Berlin Heidelberg: Springer) pp. 1–45
62. Venugopal A, Tuna F, Spaniol T P, Ungur L and Chibotaru L F 2013 *Chem. Commun.* **49** 901
63. Blagg R J, Ungur L, Tuna F, Speak J and Comar P 2013 *Nat. Chem.* **5** 673
64. Wang Y-X, Shi W, Li H, Song Y and Fang L 2012 *Chem. Sci.* **3** 3366
65. Gendron F, Pritchard B, Bolvin H and Autschbach J 2015 *Dalton Trans.* **44** 19886
66. Gómez-Coca S, Aravena D, Morales R and Ruiz E 2015 *Coord. Chem. Rev.* **289** 379
67. Hänninen M M, Mota A J, Aravena D, Ruiz E and Sillanpää R 2014 *Chem. Eur. J.* **20** 8410
68. Oyarzabal I, Ruiz J, Seco J M, Evangelisti M and Camón A 2014 *Chem. Eur. J.* **20** 14262
69. Gómez-Coca S, Urtizberea A, Cremades E, Alonso P J and Camón A 2014 *Nat. Commun.* **5** 5300
70. Costes J P, Titos-Padilla S, Oyarzabal I, Gupta T and Duhayon C 2016 *Inorg. Chem.* **55** 4428
71. Upadhyay A, Singh S K, Das C, Mondol R and Langley S K 2014 *Chem. Commun.* **50** 8838
72. Singh S K, Gupta T and Rajaraman G 2014 *Inorg. Chem.* **53** 10835
73. Rajaraman G, Singh S K, Gupta T and Shanmugam M 2014 *Chem. Commun.* **50** 1551
74. Gupta T and Rajaraman G 2014 *J. Chem. Sci.* **126** 1569
75. Lucaccini E, Sorace L, Perfetti M, Costes J-P and Sessoli R 2014 *Chem. Commun.* **50** 1648
76. Costes J P, Titos-Padilla S, Oyarzabal I, Gupta T and Duhayon C 2015 *Chem. Eur. J.* **21** 15785
77. Das C, Vaidya S, Gupta T, Frost J M and Righi M 2015 *Chem. Eur. J.* **21** 15639
78. Singh S K, Gupta T, Ungur L and Rajaraman G 2015 *Chem. Eur. J.* **21** 13812
79. Meihaus K R, Minasian S G, Lukens W W, Kozimor S A and Shuh D K 2014 *J. Am. Chem. Soc.* **136** 6056
80. Aquilante F, Autschbach J, Carlson R K, Chibotaru L F and Delcey M G 2016 *J. Comput. Chem.* **37** 506
81. Aquilante F, De Vico L, Ferre N, Ghigo G and Malmqvist P A 2010 *J. Comput. Chem.* **31** 224
82. Duncan J A 2009 *J. Am. Chem. Soc.* **131** 2416
83. Swerts B, Chibotaru L F, Lindh R, Seijo L and Barandiaran Z 2008 *J. Chem. Theory Comput.* **4** 586
84. Veryazov V, Widmark P O, Serrano-Andres L, Lindh R and Roos B O 2004 *Int. J. Quantum Chem.* **100** 626
85. Karlstrom G, Lindh R, Malmqvist P A, Roos B O and Ryde U 2003 *Comput. Mater. Sci.* **28** 222
86. Malmqvist P A, Roos B O and Schimmelpfennig B 2002 *Chem. Phys. Lett.* **357** 230
87. Chibotaru L F and Ungur L 2012 *J. Chem. Phys.* **137** 064112
88. Ungur L and Chibotaru L 2006 In *The computer programs SINGLE_ANISO and POLY_ANISO* (Leuven: University of Leuven)
89. Frisch M J, Trucks G W, Schlegel H B, Scuseria G E, Robb M A, Cheeseman J R, Scalmani G, Barone V, Mennucci B, Petersson G A, Nakatsuji H, Caricato M, Li X, Ratchian H P, Izmaylov A F, Bloino J, Zheng G, Sonnenberg J L, Hada M, Ehara M, Toyota K, Fukuda R, Hasegawa J, Ishida M, Nakajima T, Honda Y, Kitao O, Nakai H, Vreven T, Montgomery J A Jr, Peralta J E, Ogliaro F, Bearpark M, Heyd J J, Brothers E, Kudin K N, Staroverov V N, Kobayashi R, Normand J, Raghavachari K, Rendell A, Burant J C, Iyengar S S, Tomasi J, Cossi M, Rega N, Millam N J, Klene M, Knox J E, Cross J B, Bakken V, Adamo C, Jaramillo J, Gomperts R, Stratmann R E, Yazyev O, Austin A J, Cammi R, Pomelli C, Ochterski J W, Martin R L, Morokuma K, Zakrzewski V G, Voth G A, Salvador P, Dannenberg J J, Dapprich S, Daniels A D, Farkas Ö, Foresman J B, Ortiz J V, Cioslowski J and Fox D J 2009 In *Gaussian 09, Revision D.01* (Wallingford CT: Gaussian, Inc.)
90. Cundari T R and Stevens W J 1993 *J. Chem. Phys.* **98** 5555
91. Schafer A, Huber C and Ahlrichs R 1994 *J. Chem. Phys.* **100** 5829
92. Becke A D 1993 *J. Chem. Phys.* **98** 5648
93. Lee C, Yang W and Parr R G 1988 *Phys. Rev. B.* **37** 785
94. Stephens P J, Devlin F J, Chabalowski C F and Frisch M J 1994 *J. Phys. Chem.* **98** 11623
95. Bader R F W 1990 In *Atoms in molecules—A Quantum Theory* (Oxford, UK: Oxford University Press)
96. Bader R F W 2009 *J. Phys. Chem. A* **113** 10391
97. BieglerKönig F and Schönbohm J 2002 *J. Comput. Chem.* **23** 1489
98. Chilton N F, Collison D, McInnes E J L, Winpenney R E P and Soncini A 2013 *Nat. Commun.* **4** 2551
99. Espinosa E, Alkorta I, Elguero J and Molins E 2002 *J. Chem. Phys.* **117** 5529
100. Jenkins S and Morrison I 2000 *Chem. Phys. Lett.* **317** 97
101. Jabłoński M 2015 *J. Phys. Chem. A* **119** 11384
102. Jabłoński M 2015 *J. Phys. Chem. A* **119** 4993
103. Popelier P and Logothetis G 1998 *J. Organomet. Chem.* **555** 101
104. Tognetti V, Joubert L, Raucoules R, De Bruin T and Adamo C 2012 *J. Phys. Chem. A* **116** 5472